

9B.3

Prediction of Convective Initiation and Storm Evolution on 12 June 2002 during IHOP_2002. Part I: Control Simulation and Sensitivity Experiments

Haixia Liu and Ming Xue

Center for Analysis and Prediction of Storms and School of Meteorology
University of Oklahoma, Norman OK 73072

1. Introduction

During the warm season over the Southern Great Plains (SGP) of the United States, strong convective storms are responsible for a large portion of the annual rainfall. Accurate prediction of quantitative precipitation associated with these warm season systems has been a particularly elusive task (Fritsch and Carbone 2004). The prediction of the exact timing, location and intensity of convective initiation and the subsequent evolution of the convective systems are even more difficult. Such difficulties arise in part from the poor knowledge of four-dimensional water vapor distribution with high temporal and spatial variability, inadequate understanding of the convective initiation (CI) processes and the inability of typical numerical models to accurately represent important physical processes. To address some of these questions, the International H₂O Project (IHOP_2002, Weckwerth et al. 2004) field experiment was carried out in the spring of 2002.

Weckwerth and Parsons (2006) present a review on convective initiation, in particular, that by surface boundaries prevalent in the SGP environment. Wilson and Roberts (2006) systematically summarize all CI events and their evolution during the IHOP period, based on observational data. The ability of the operational 10-km Rapid Update Cycle (RUC) (Benjamin et al. 2004) in predicting these events is also briefly discussed. Xue and Martin (2006a; 2006b, hereafter XM06a and XM06b respectively or XM06 for both) present a

detailed numerical study on the 24 May 2002 dryline CI case.

In XM06, the Advanced Regional Prediction System (ARPS, Xue et al. 2000; Xue et al. 2001; Xue et al. 2003) and its data assimilation system were employed to simulate the events at 3 and 1 km horizontal resolutions. Accurate timing and location of the initiation of three initial convective cells along the dryline are obtained in the model at the 1 km resolution. Through a detailed analysis on the model results, a conceptual model is proposed in which the interaction of the fine-scale boundary-layer horizontal convective rolls (HCRs) with the mesoscale convergence zone along the dryline is proposed to be responsible for determining the exact locations of convective initiation. Worth noting in this case is that the CI did not occur at the intersection point between the dryline and a southwest-northeast-oriented surface cold front located in the north, or at the dryline-cold front 'triple point', which conventional wisdom would highlight as the location of highest CI potential. In fact, most of the observing instruments were deployed around the triple point that day, missing the true CI that actually occurred further south along the dryline.

Another CI event that was extensively observed during IHOP_2002 is that of 12 June 2002, which also involved a dryline intersecting a cold front. Further complicating the situation was a cold pool and the associated outflow boundary that ran roughly east-west and intercepted both cold front and dryline near its west end. In the afternoon of 12 June, CI

occurred along and near the dryline, and along and near the outflow boundary. Some of these storm cells organized into a squall line into the evening and propagated through the central and northeast part of Oklahoma through the night, producing damaging wind gust, hail and heavy precipitation. On this case, Weckwerth et al. (2005) performed a preliminary observation-based study that employed multiple datasets and discussed pre-convective, clear-air features and their influence on convective initiation. This case is also one of the two highlighted in the survey study of Wilson and Roberts (2006). Because of the limitations of the observational data sets, the CI mechanisms of this case could only be hypothesized in these two observation-based studies. For the same case, Markowski et al. (2006) analyzed the ‘convective initiation failure’ in a region near the intersection of the outflow boundary and dryline. Data from multiple mobile Doppler radars were used in their analysis. This region was chosen for intensive observations because of its proximity to the outflow-boundary–dryline intersection point (similar to a triple point) but the actual initiation occurred about 40 km to the east and to the south along the dryline. Clearly, a better understanding of the CI mechanisms in this and other cases, and improvement in NWP model prediction skills, are much needed.

In this study, a similar approach to that employed in XM06 is used to study the CI processes and subsequent storm evolutions in the 12 June, 2002 case. Additional numerical experiments are also conducted to evaluate the impact of various model and data assimilation configurations. As in the study of XM06, 3 km and 1 km horizontal resolution grids are used, and the results of this study will be presented in two parts. In this first part (Part I), an overview of the case is presented, together with a brief description of the numerical model and its configurations, and of the data assimilation method and observation data used. This part will focus on the results of the 3 km grid, and examine, through a set of sensitivity

experiments, the impact of a number of model and data assimilation configurations on the prediction of CI and storm evolution. In the second part of this paper (Part II, Xue and Liu 2007), a detailed analysis of the results of the 1 km grid will be presented, with the primary goal of understanding the exact processes responsible for the CI.

The rest of this paper is organized as follows. In section 2, we discuss the synoptic and mesoscale environment of the 12 June 2002 case, the sequence of storm initiations along the dryline and the outflow boundary, and the subsequent evolution of these cells and their eventual organization into a squall line. Section 3 introduces the numerical model used and its configurations, as well as the design of actual experiments. The results are presented and discussed in sections 4 and 5 and a summary is given in section 6.

2. Overview of the 12 June 2002 case

As pointed out in the introduction, the case of 12 June, 2002 is a complicated one that involves a number of mesoscale features that interact with each other. Figure 1 shows the surface observations superposed on visible satellite imagery at 2045 UTC (all times are UTC unless otherwise noted) or 1445 LST, 12 June 2002 in the IHOP domain. There was an outflow left behind by a mesoscale convection system (MCS) earlier that day, located over southern Kansas (KS), northeastern Oklahoma (OK) and northwest Arkansas (AR). The southern boundary of this outflow (indicated by the dashed line in Fig. 1) stretched from far northwest OK to the northwest AR, separating the warm, moist, generally southerly flow to its south from the cool, but moist, easterly and southeasterly flow to the north of the boundary. During the day, this boundary receded to the north, acting more like a warm front. A weak cold front extended from the eastern OK panhandle (at the western end of the outflow boundary) toward the south-southwest to the central Texas (TX) panhandle. A dryline was

present at the same time, oriented northeast-southwest from the eastern OK panhandle to the southwestern TX panhandle and intersected the cold front at the central TX panhandle (at the southern end of the cold front). Warm dry air existed west of the dryline and ahead of the cold front where southwesterly winds dominated. Behind the cold front, most of the winds came from the north or north-northeast. The low-level winds showed the existence of a mesoscale cyclone west of the dryline-outflow boundary triple point (see, e.g., Fig. 5d). Another feature worth pointing out is a region east of the dryline with generally southerly surface winds exceeding 15 knots which provided ample moist air for CI near the dryline and outflow boundary. Shown in Fig. 2 is the surface convective available potential energy (CAPE, Fig. 2a) and convective inhibition (CIN, Fig. 2b) at 2200, adapted from Wilson and Roberts (2006). The CAPE maximum of over 5000 J kg^{-1} and CIN values near or lower than 15 J kg^{-1} were located along the outflow boundary. Near the intersection of the cold front and the dryline, as well as along the southwest portion of dryline, the CAPE was over 3000 J kg^{-1} and CIN was smaller than 15 J kg^{-1} . These three regions were considered the preferred CI locations based on these data.

Fig. 3 shows the multi-radar mosaic of composite (vertical column maximum) reflectivity as produced by the procedure of Zhang et al. (2005) at 2130, 0000, 0100, 0300, which are the times when most storms were initiated, and when the squall line was starting to organize, intensifying, and maturing, respectively. The first group of convective cells in Fig. 3 was initiated at about 1900 near the TX-New Mexico (NM) border (denoted '1a' in Fig. 3a). One hour later (2000), the second cell group (denoted as '1b' in Fig. 3a) was initiated 100 km north of group '1a'. Group '1a' was

ahead of the dryline while group '1b' was right over the southern extent of the dryline. During the next 40 minutes, more convective cells (denoted as '1c' in Fig. 3a) were initiated near these two groups. These regions were favorable for CIs as suggested by Fig. 2. At about 2030, near the intersection of the cold front and dryline near Amarillo, TX, another group of convective cells (denoted as '2' in Fig. 3a) was initiated and intensified quickly, leading to hail reports and strong winds along their gust fronts. During the next hour, additional convective cells formed, along the northern extent of the dryline (denoted as group '3') and near, but south of, the outflow boundary (denoted as group '4'). Further east along the outflow boundary, group '5' is found which was initiated at around 2000 (Fig. 3a). By 0000 of 13 June (Fig. 3b), these cells reorganized into somewhat different cell groups, denoted as 'A', 'B', 'C', '4' and '5'. Group A is basically the group evolved from '1a', and 'B' is a combination of groups '1b', '1c' and the southern part of '2' that underwent splitting during the period. Group 'C' was made up of the northern part of '2' and '3' while groups '4' and '5' maintained their identities. Between 2130 and 0000, more cells developed north of the OK-KS border (Fig. 3b). During the hour after 0000, cell groups 'A', 'B' and 'C' either weakened or nearly dissipated, while group '4' extended further westward into the eastern OK panhandle and group '5' grew in size (Fig. 3c). In the next 2 hours, groups '4' and '5', together with other cells between them and further to the east, became connected and organized into a solid squall line (Fig. 3d) which continued its propagation southeastward for the next 3 hours until around 0600. The more detailed processes involved in the cell initiation and evolution will be discussed in the next two sections, together with the model simulations of these processes.

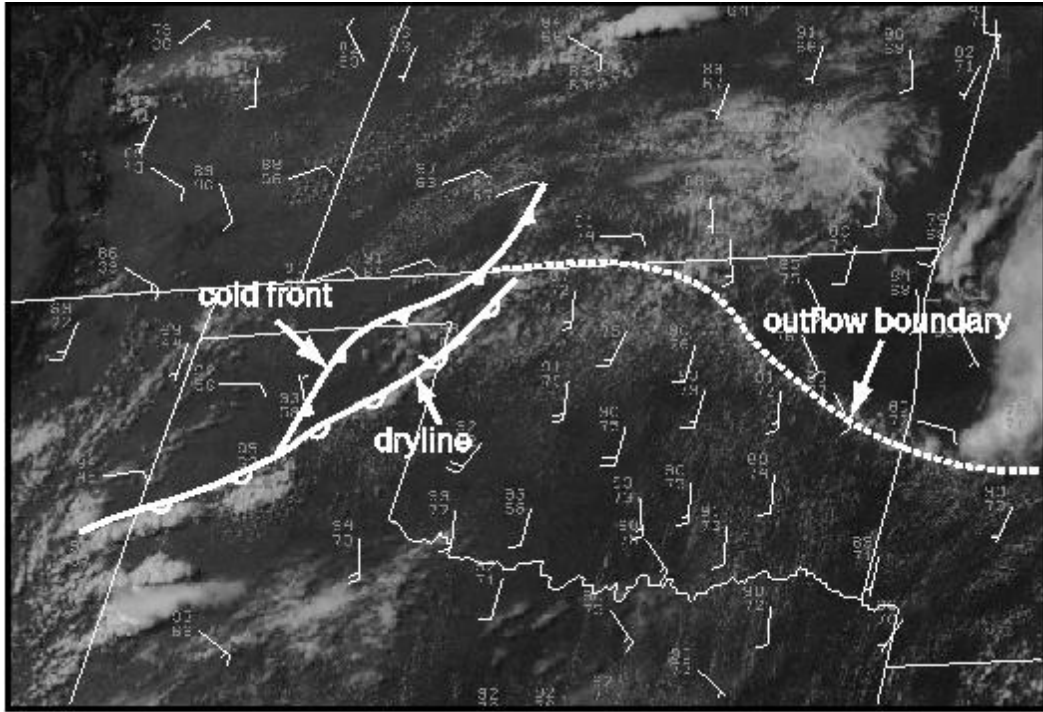


Fig. 1. Visible satellite imagery at 2045 UTC, 12 June, 2002, with surface observations overlaid. Station models show wind barbs in knots (with one full barb representing 10 knots), and temperature and dew point temperature in Fahrenheit.

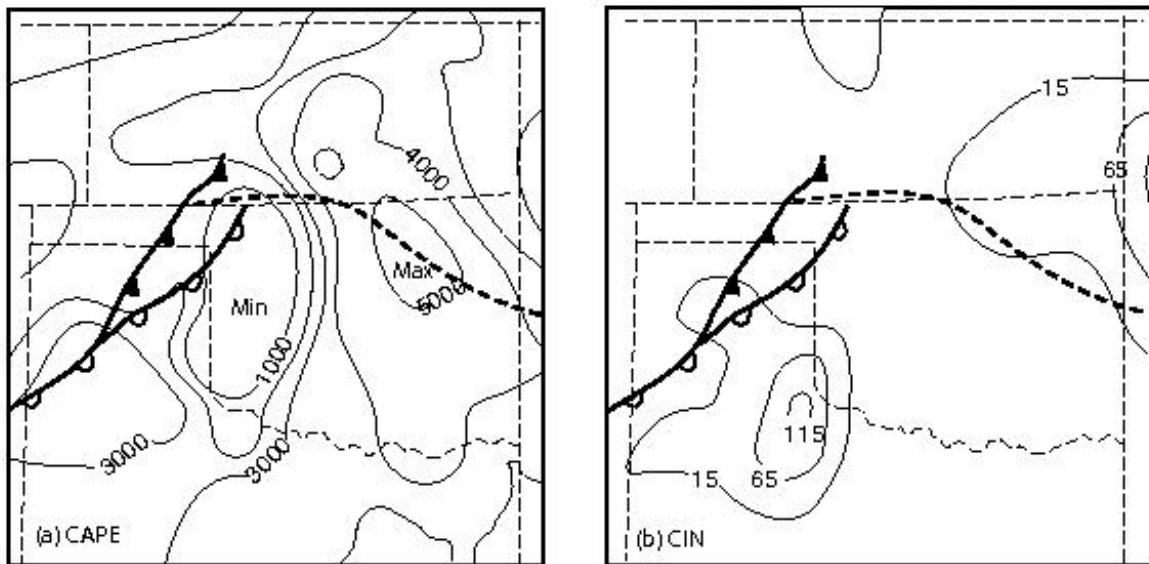


Fig. 2. (a) CAPE (contour interval of 1000 J kg^{-1}) and (b) CIN (first contour at 15 J kg^{-1} with contour interval of 50 J kg^{-1}) at 2200 UTC, 12 June, 2002 (adapted from Wilson and Roberts 2006).

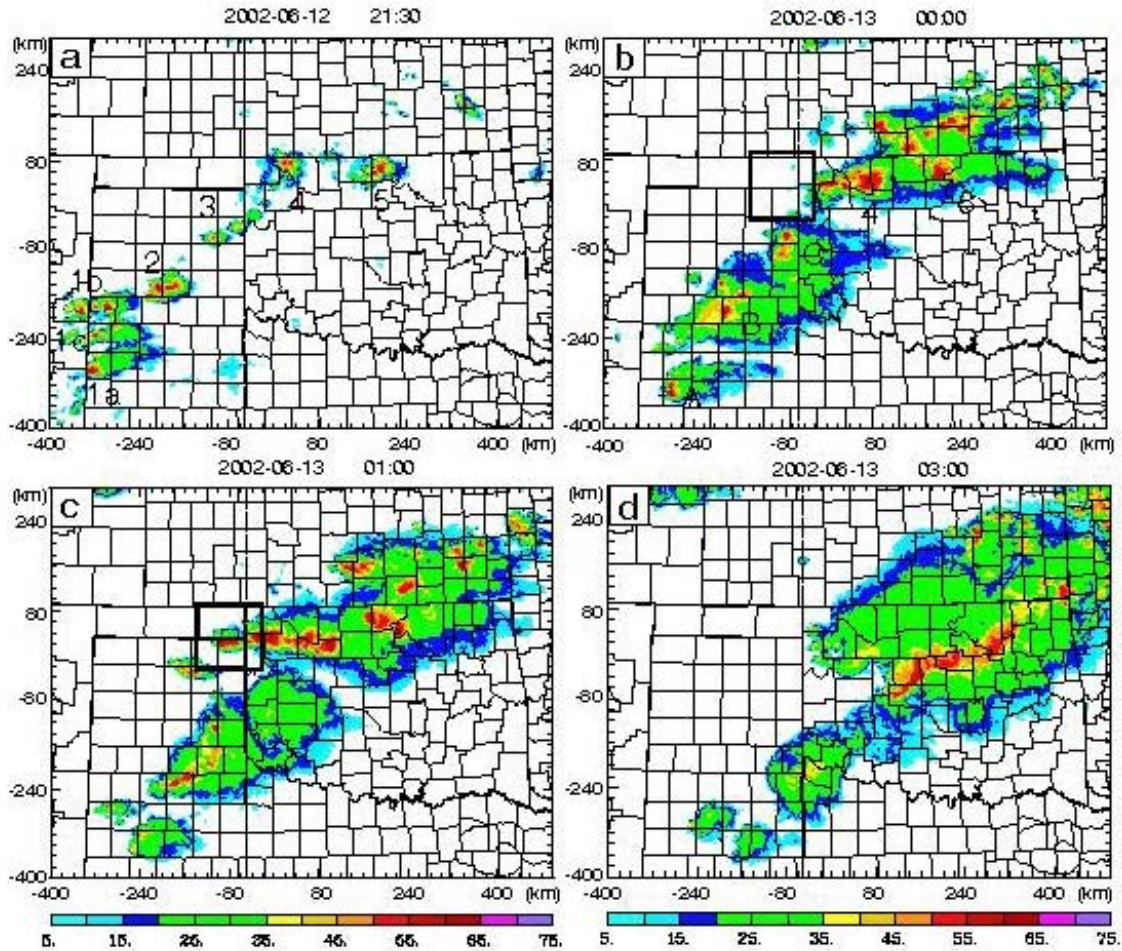


Fig. 3. Observed composite reflectivity mosaic at (a) 2130 12 June, (b) 0000, (c) 0100, and 0300 13 June, 2002. The letters 1a, 1b, 1c, 2, 3, 4 mark the CI locations. The black squared box in panels (b) and (c) corresponds to the small zoomed-in domain shown in Fig. 9.

3. Numerical model, data and experiment design

As in XM06, version 5 of ARPS (Xue et al. 2000; 2001; 2003) is used in this study. The ARPS is a nonhydrostatic atmospheric prediction model formulated in a generalized terrain-following coordinate. As in XM06, two one-way nested grids at 3 and 1 km horizontal resolutions, respectively, are used. In the vertical, the grid spacing increases from about 20 m near the ground to about 800 m near the model top that is located about 20 km above sea level. The 3 km resolution is believed to be high enough to resolve important mesoscale

structures while 1 km resolution is necessary to begin resolving smaller convective structures, including the boundary layer horizontal convective rolls and individual cells of deep moist convection.

The model terrain and land surface characteristics on the 3 and 1 km grids are created in the same way as in XM06. The lateral boundary conditions (LBCs) for the 3 km grid are from time interpolations of 6-hourly NCEP (National Centers for Environmental Prediction) Eta model analyses and the 3-hour forecasts in-between the analyses, while the 1 km grid gets its LBCs from the 3 km forecasts at 10 minute intervals.

In this study, the results of numerical simulations are found to be sensitive to the lateral boundary locations of the 3 km grid, and the domain of the 3 km grid used in our control simulation (see Fig. 4) is much larger than that used in XM06. The impact of the domain size and boundary locations will be specifically discussed in section 5c.

The ARPS is used in its full physics mode (see Xue et al. 2001, 2003). The 1.5-order TKE-based subgrid-scale turbulence

parameterization and TKE-based PBL-mixing parameterization (Sun and Chang 1986; Xue et al. 1996) are used. The microphysics scheme is the Lin et al. (1983) 3-ice microphysics. The National Aeronautics and Space Administration Goddard Space Flight Center (NASA GSFC) long and short-wave radiation package (Chou 1990, 1992; Chou and Suarez 1994) is used and the land surface condition is predicted by a two-layer soil-vegetation model initialized using the state variables presented in the Eta analysis.

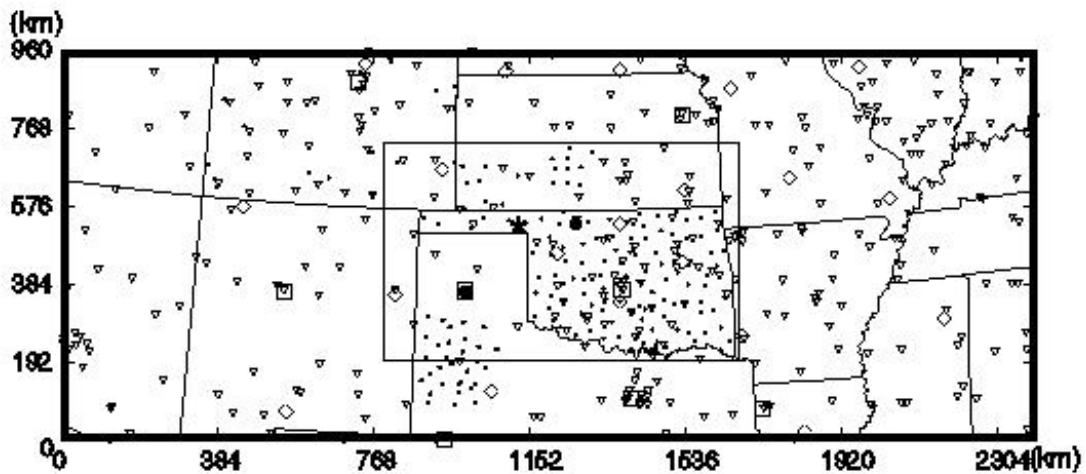


Fig. 4. The 3 km model domain used by all experiments except for SML, which uses the smaller domain shown by the rectangle in the figure. The stations of the Oklahoma Mesonet, the West Texas Mesonet, the southwest Kansas mesonet, the Kansas ground water management district # 5 network, and the Colorado agricultural meteorological network are marked by small dots; the stations from ASOS and FAA surface observing network (SAO) are marked by downward triangles; the stations from the NWS radiosonde network are marked by squares; and the stations from the NOAA wind profiler network are marked by diamonds. Two filled circles mark the locations of KVNK and KAMA WSR-88D radars in Oklahoma and Texas respectively. The filled star represents the S-Pol radar station.

The initial conditions of our numerical simulations are created using the ARPS Data Analysis System (ADAS, Brewster 1996), in either the cold-start mode where the analysis is performed only once using an Eta analysis as the background, or with intermittent assimilation cycles where ARPS forecasts from the previous forecast cycles are used as the background for the cycled analyses. For all experiments to be presented, the initial

conditions, created with or without assimilation cycles, are valid at 1800, 12 June, about 1 hour preceding the first observed convective initiation near the dryline. As one of the intensive observation days of IHOP_2002 with convective initiation study as the mission goal, various remote sensing instruments were deployed on that day, in addition to routine and special conventional observations (Weckwerth et al. 2004). In this study, conventional forms of

data are assimilated into the model initial condition, including those of (regular and mesonet) surface stations, upper-air soundings and wind profilers. Available aircraft data (MDCRS) are also included. Table 1 lists the standard and special data sets used, together with their key characteristics. Data from the

IHOP-deployed National Center for Atmospheric Research S-band polarimetric (NCAR S-pol) radar and from the Weather Surveillance Radar 88 Doppler (WSR-88D) radars in the region are used extensively for verification, especially KVNIX (Enid, OK) and KAMA (Amarillo, TX) radars (see Fig. 4).

Type of dataset	Abbreviation	description	Temporal resolution	Special or standard	Number of stations
Upper-air datasets	raob	National Weather Service (NWS) radiosonde network	3 hour	data at 1200 are standard, others are considered special	18 at 1200; 10 at 1500 and 1800
	wpdn	Wind Profiler Demonstration Network	1 hour	standard	20
	comp*	special composite data set composed of many upper-air observing networks	1 hour	special	1
	mdcrs	NWS Meteorological Data Collection and Reporting System aircraft observations	1 hour	special	varies
Surface datasets	sao	Surface observing network composed of the Automated Surface Observing System (ASOS) and the Federal Aviation Administration's (FAA) surface observing network.	1 hour	standard	about 250
	coag	Colorado Agricultural Meteorological Network	1 hour	special	29
	okmeso	OK Mesonet	1 hour	special	About 125
	swks	Southwest Kansas Mesonet	1 hour	special	8
	gwmd	Kansas Ground Water Management District # 5 Network	1 hour	special	10
	wtx	West Texas Mesonet	1 hour	special	30

* A description on the individual networks included in the composite can be found in Stano (2003).

Table 1. List of the abbreviations of the observation networks used in this study and some of their characteristics.

After an initial condition is obtained at 1800 on the 3 km grid, the ARPS model is integrated for 9 hours until 0300, 13 June, 2002, the mature time of the squall line system. The 1 km grid forecast also starts at 1800, with the initial condition interpolated from the 3 km grid, and runs until the same ending time. As

pointed out earlier, we will present only the results from 3 km experiments in this part (Part I). The results of 1 km grid experiments, together with detailed analyses on the convective initiation mechanisms, will be presented in Part II.

In addition to a control simulation, we perform a set of sensitivity experiments at 3 km resolution to examine the impact of intermittent data assimilation cycles and IHOP special data, the effect of vertical correlation scales used in the ADAS, and the effect of lateral boundary locations (Table 2). In all ADAS analyses, five analysis passes are performed, with each pass including different sets of data and using different spatial correlation scales. Table 3 lists the observations analyzed and the correlation

scales for the horizontal and vertical for each analysis pass used in all experiments unless otherwise noted. Using one more pass than in XM06, the horizontal correlation scale starts at a value slightly larger than that in XM06, and ends at a value that is smaller. The vertical correlation scales are generally smaller than the corresponding ones used in XM06. These correlation scales were chosen based on additional experiments performed after the study of XM06 for the 24 May, 2006 case.

Experiment	Assimilated data	Assimilation interval	CI1a	CI2	CI3	CI4
			Time of CI in model Position error			
CNTL	all data	1 hour	2040 40 km SW	2040 < 5 km	2250 60 km NE	2130 20 km NE
COLD	all data	single analysis at 1800	Missing	Missing	2120 < 10 km	Missing
3HRLY	all data	3 hours	2030 40 km SW	2040 < 5 km	2200 70 km NE	2050 15 km NE
6HRLY	all data	6 hours	2030 60 km SW	2100 < 5 km	2140 70 km NE	2050 50km NE
STDOBS	standard data only	1 hour	2050 40 km SSW	2030 10 km E	2140 < 10 km	2040 5 km E
ZRANGE	all data	1 hour	2030 100 km SW	2000 < 5 km	2220 70 km NE	2100 5 km N
SML	all data	1 hour	1940 10 km N	2010 10 km NE	2240 70 km NE	2110 20 km N
Time of observed initiation			1900	2030	2130	2100

Table 2. Table of numerical experiments and their characteristics. CI1a, CI2, CI3, and CI4 refer to the convective initiation near the southwest most portion of the dryline, near Amarillo, Texas, the intersection of cold front and dryline, and near Woods, Oklahoma, near the intersection of outflow boundary and dryline, corresponding to cell groups ‘1a’, ‘2’, ‘3’ and ‘4’, respectively.

Table 2 lists all numerical experiments with abbreviated names and their descriptions. The control experiment, CNTL, includes the most data (Table 1). Standard and special IHOP observations are assimilated in hourly analysis cycles over a 6 hour period that ends at 1800. CNTL is designed to capture the convective cell initiations and later evolution into a squall line. Among the other experiments, COLD uses a

cold-start analysis for the initial condition; 3HRLY uses two 3-hourly assimilation cycles while 6HRLY uses a single 6-hourly cycle. STDOBS includes only standard observations, as listed in Table 2, while ZRANGE tests the impact of different vertical correlation scales used in ADAS, and SML tests the impact of lateral boundary locations.

The performance of forecasts is evaluated by comparing the timing and locations of the initiations of convective cells along and near the dryline and the outflow boundary against radar observations. The structure and evolution of the model storms and their later organization into a squall line are examined by comparing predicted and observed reflectivity fields.

4. Results of the control experiment

Fig. 5a - d shows the analyzed surface fields of wind and water vapor mixing ratio during the 6-hour assimilation cycle from 1200 through 1800 for experiment CNTL. A dryline indicated by a moisture gradient is quickly formulated as shown in panel b and moves eastward shown in panels c and d. The wind shift exists along the dryline. Fig. 5e shows the analyzed fields of temperature at the surface and mean sea level pressure at 1800 the end of assimilation cycle for CNTL. This figure panel indicates strong surface heating and the formation of a mesoscale low center near eastern OK panhandle (marked by capital letter L). The MCS outflow (the cold center at northeast OK corner) is clearly evident in this panel as well. The wind shift line along the outflow boundary is present; wind convergence is found along this line (dashed line in panel e). This outflow boundary is also marked in panel d. It can be seen that north of the boundary, especially near the central OK-KS border, moisture is enhanced. To the south of the boundary and east of the dryline, strong southerly winds with speeds between 5 and 10 m s^{-1} exist at the surface, with the strongest winds being located in western OK and central

TX; they bring rich moisture into the region and provide a favorable environment for CI and for the establishment of a squall line later on.

Fig. 6 shows the fields of temperature and wind vectors at 850 hpa to illustrate the cold front and mesolow circulation as well. In the middle of the dryline (Fig. 5d), the convergence straddles the zone between the cold front and dryline. Meanwhile, significant fine-scale structures exist in the surface moisture field, as indicated by the wiggles on the specific humidity contours. These are related to the boundary layer (dry) convective structures that develop due to surface heating, and are generally of smaller scales than can be captured by the surface observation networks. In fact, such details are absent in the single-time analysis of cold-start experiment COLD (Table 2), and most of the gradients are also weaker in that analysis (not shown).

In general, the prediction of convective initiation in CNTL is good. Fig. 7 depicts the forecast fields of water vapor mixing ratio and winds at the surface, and the composite (vertical column maximum) radar reflectivity at 2130, 12 June, 2002 and at 0000, 0100 and 0300 of 13 June, which can be compared directly to those in Fig. 3.

The model predicts the convective initiation at the intersection of the cold front and dryline near Amarillo, TX (denoted as '2' in Fig. 3a or CI2 in Table 2) remarkably well. The model convection is initiated around 2040 and shows up as fully developed cells at 2130 (marked by '2' in Fig. 7a). The location of this group of cells is almost exact and initiation timing error is about 10 minutes.

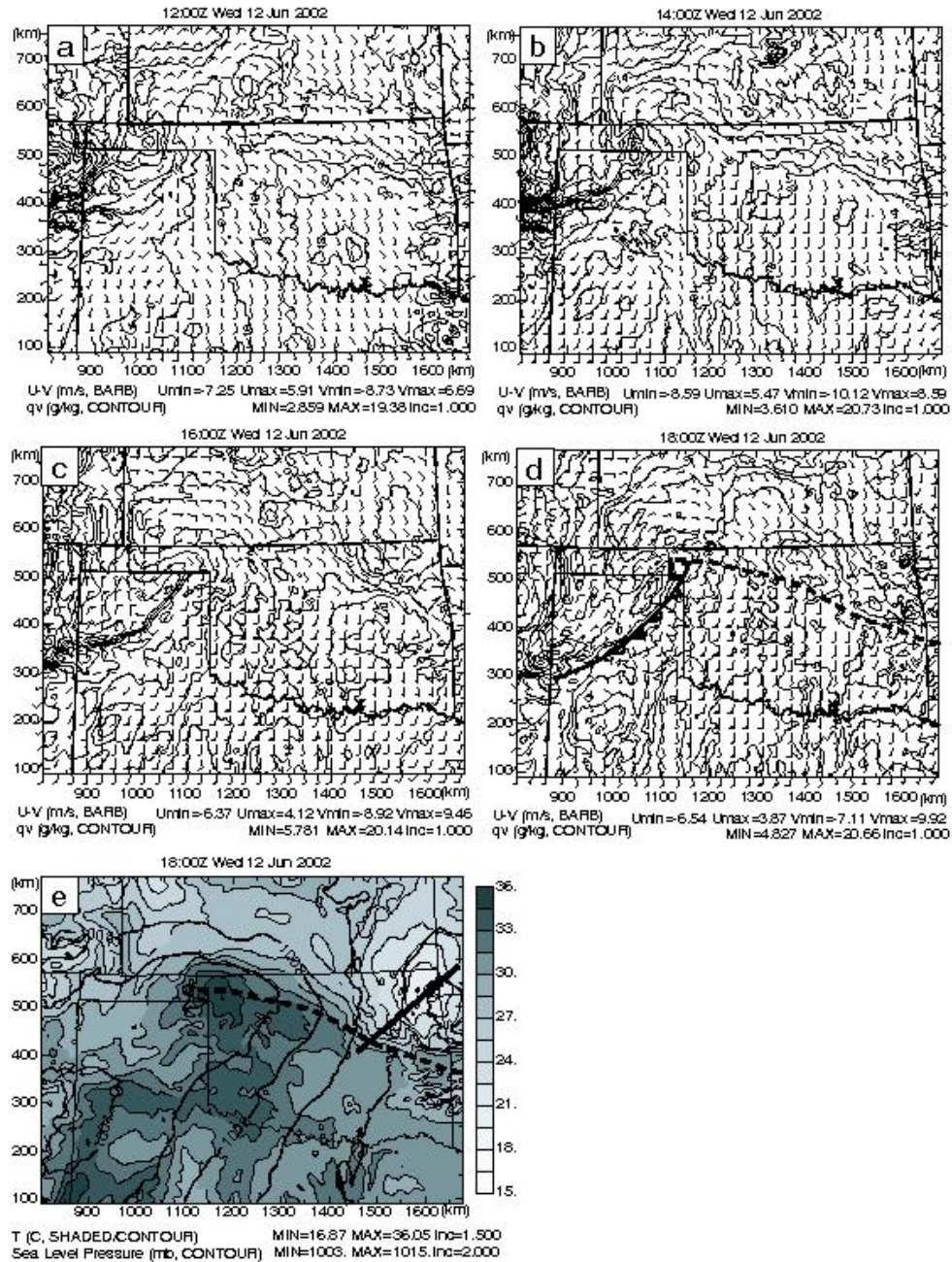


Fig. 5 The surface fields of water vapor mixing ratio (contours, g kg^{-1}) and the wind vector (full barb represents 5 m s^{-1} , half barb 2.5 m s^{-1}) from ADAS analysis at (a) 1200 UTC, (b) 1400 UTC, (c) 1600 UTC, (d) 1800 UTC 12 June 2002, (e) the temperature field at the surface (gray shading plus thin black contours, $^{\circ}\text{C}$) and the mean sea level pressure (thick black contours, hPa) at 1800 UTC 12 June 2002. In panel (d), the dryline is marked by standard symbol. In panel (e), the thick straight black line indicates the vertical cross-section shown in Fig. 12. In both panels (d) and (e), the thicker dashed line marks the MCS outflow boundary.

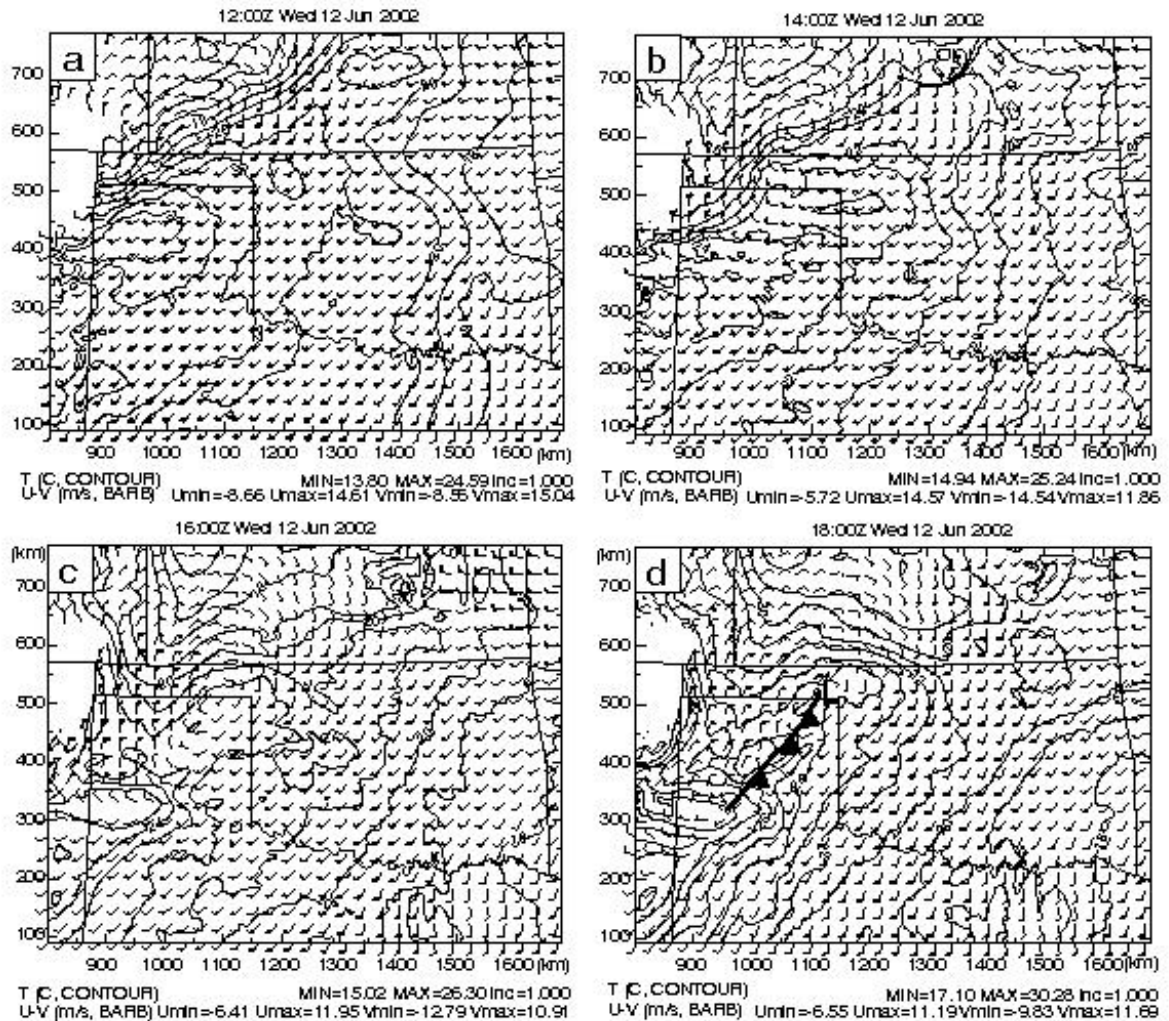


Fig. 6 The fields of temperature (contours, °C), and the wind vector (full barb represents 5 m s^{-1} , half barb 2.5 m s^{-1}) at 850 hpa level from ADAS analysis at (a) 1200 UTC, (b) 1400 UTC, (c) 1600 UTC, (d) 1800 UTC 12 June 2002. In panel (d), the cold front is marked by standard symbol.

For the groups of cells denoted as ‘1a’, ‘1b’ and ‘1c’ in Fig. 3a, the situation is more complicated. In the real world, these cells were initiated over a period of about 1.5 hours, starting at 1900, as described in section 2. The cells along the dryline, marked by ‘1b’ in Fig. 3a, were initiated around 2000. In the model, there are not three separate groups of cells as observed. A group of cells is initiated along the TX-NM border, south of the dryline at around 2040, at roughly the location of observed group ‘1a’. At 2130 (Fig. 7a), this group matches very well the observed cells in location (Fig. 3a).

The cells associated with observed group ‘1b’ are much weaker in the model and are located further east along the dryline, but still separate from observed ‘2’ (Fig. 3a), especially as earlier times (not shown). Despite these discrepancies, the overall behavior of model forecast in this region is still quite good.

Additional convective cells along the northern part of the dryline (group ‘3’ in Fig. 3a) also developed in CNTL, but at a later time between 2240 and 2300 (not shown) or about 1.5 hours later than the observations. They are marked as ‘(3)’ in Fig. 7a where ‘()’ indicates

that the cells do not yet exist at this time. In the real world, part of cell group '2' merged with group '3' between 2130 and 0000 to form the group marked by 'C' in Fig. 3b, located on the west side of the western OK-TX border. In the

model, a similar process occurred during this period and the model group 'C' is located off to the east side of the same OK-TX border (Fig. 7b), giving rise to a location error of less than half a county or about 30 km.

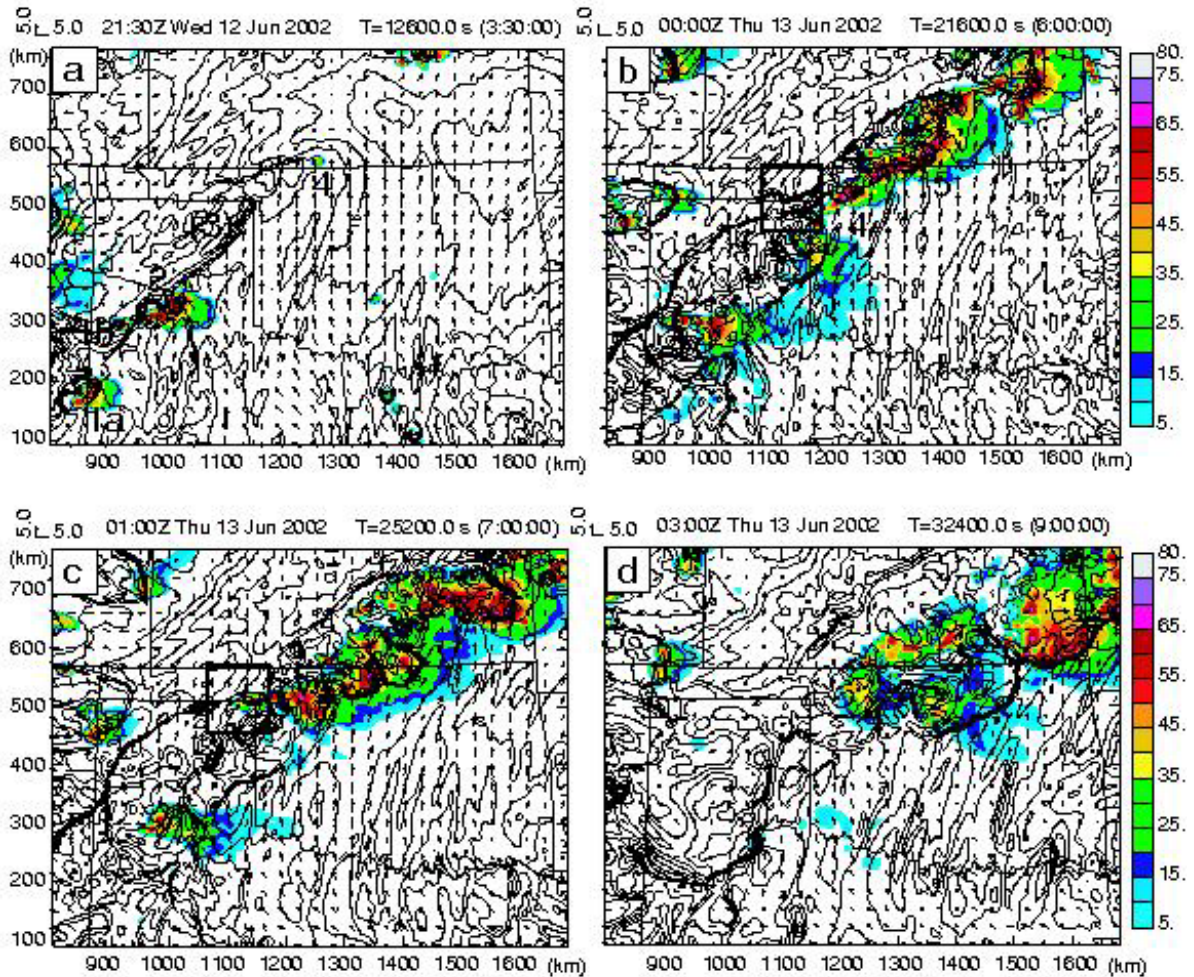


Fig. 7. The forecasted surface fields of water vapor mixing ratio (contours, contour interval is 1.0 g kg^{-1}), the wind vector (m s^{-1}) and composite reflectivity (shaded, dBZ) at (a) 2130, 12 June, 2002 (b) 0000, (c) 0100 and (d) 0300, 13 June, 2002 from CNTL run. The number 1, 2 and 4 in (a) indicate the locations of three primary convective cells. The black squared box in (b) and (c) corresponds to the small zoomed-in domain shown in Fig. 9.

In the model, a small cell starts to become visible at 2130 ('4' in Fig. 7a) that corresponds to the observed group '4' near the OK-KS border. The observed cell '4' had a similar intensity as this model cell in terms of radar echo at around 2110 and reached 55 dBZ

intensity by 2130 (Fig. 3a); there is therefore a time delay of 20 to 30 minutes in the model with this cell. The model initiation occurred about 20 km northeast of the observed one. This cell does occur in the model to the south of the surface wind shift and convergence line and to

the east of the dryline, as was observed by radar which can identify the dryline and convergence line as reflectivity thin lines (not shown).

The evolution of the model predicted reflectivity pattern is similar to that observed. In the real world, cell group '2' split at around 2150, with the southern part merging with groups '1b' and '1c' to eventually form group 'B' and the northern part merging with group '3' to form group 'C' (Fig. 3b). Group '1a' remained by 0000 of June 13 (Fig. 3b). In the model, the splitting of group '2' started to occur at around 2140 with some sign of splitting visible at 2130 (Fig. 7a); the northern part moved northeastward and merged with some much weaker cells in the model (model group 3) that developed along the northern portion of the dryline to form group 'C'. Group 'C' gained its maximum echo intensity of almost 70 dBZ near Amarillo, TX at around 2330, the same time observed reflectivity reached maximum intensity, then started to weaken. By 0000, when it crossed the western OK border, it was already rather weak; it dissipated quickly afterwards. Such an evolution is very similar to the observed one. As pointed out earlier, the peak intensity of the observed group 'C' also occurred before 0000 (the time of Fig. 3b), at around 2330.

In the model, the southern part of the split group '2' moved south-southeastward slowly and merged with the northeastward propagating group '1', at around 2350 to form group 'B' seen in Fig. 7b. This group then died out gradually over the next three hours (Fig. 7c and d).

Almost all cells that were initiated along the dryline dissipated by 0300, June 13, both in the real world (Fig. 3d) and in the model (Fig. 7d). The main development between 0000 and 0300 June 13 occurred along the outflow boundary close to the OK-KS border, and the storm cells there eventually organized into a squall line by 0300 (Fig. 3d). Actually, cell groups '4' and '5' found at 2130 (Fig. 3a) represent the origin of the final organized squall

line system. These cells formed just south of (group '4') or along (group '5') the outflow boundary, and intensified (Fig. 3b) and merged with new cells that developed over the ensuing few hours near the convergence boundary, as well as with cells that formed east of the dryline in northwest OK before 0000. In the model, cell group '4' is found at a similar location as the observed counterpart at 0000 (Fig. 7b) while the modeled group '5' is located further north than the observed, and exists in the form of a connected line rather than more discrete cells. The group of cells in a northeast to southwest oriented line north and northeast of group '5' seems to also match the observations well at this time. In the model, these cells apparently formed near the convergence boundary that had been pushed northward across the OK-KS border by the strong southerly flow. A similar development appears to have occurred in the real world too, based on more frequent radar maps (not shown).

By 0000, observed cell group '4' had already gained an elongated east-west orientation (Fig. 3b). During the next hour, this 'line' extended westward by about 100 km (Fig. 3c) through the initiation of new cells. The initiation of these cells in a region behind the dryline was actually due to the collision between the original outflow boundary and the northwestward propagating gust front from the earlier dryline convection. Such a process is most clearly seen in the low-level reflectivity fields of the NCAR S-pol radar deployed in the OK panhandle during IHOP. In Fig. 8, the gust fronts and the convergence lines are seen clearly as thin lines with enhanced reflectivity. At 2303, two outflow boundaries are clearly visible ((Fig. 8a) and by 0006 (Fig. 8b), the eastern portion of the gust front, in a bow shape, has just collided with the northern outflow boundary, starting to produce new cells indicated by the large open arrow. The western, stronger, bow-shaped gust front was advancing and spreading rapidly and collided before 0006 with the eastern bow-shaped gust front,

producing a cell indicated by double solid arrows. But 0036, only 30 minutes later, this western portion has also collided with the northern outflow boundary, triggering and leaving right behind the gust front a new cell, indicated by the large black arrow (Fig. 8c). By 0100, this cell and the one formed earlier to the east, i.e., the two indicated by the two large arrows, reached their full strength and started to merge laterally (Fig. 8d).

indicated by the large black arrow (Fig. 8c). By 0100, this cell and the one formed earlier to the east, i.e., the two indicated by the two large arrows, reached their full strength and started to merge laterally (Fig. 8d).

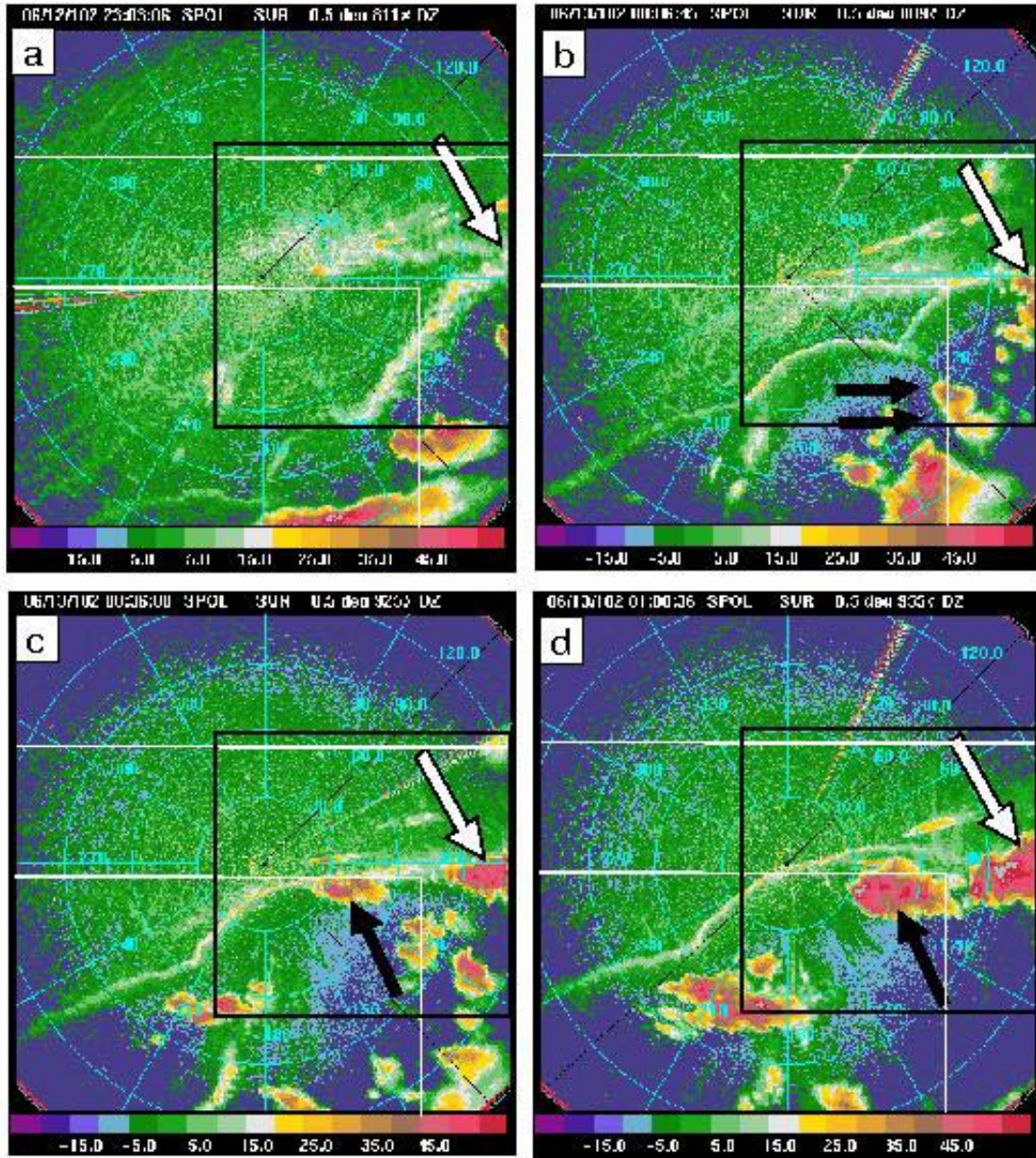


Fig. 8. The S-Pol radar reflectivity observations at 0.5 degree elevation angle at (a) 2303, 12 June 2002, (b) 0006, (c) 0036 and (d) 0100, 13 June 2002. The large black box in each panel indicates the domain shown in Fig. 9 and the arrows point to the locations of convective cells triggered by collisions of outflow boundaries.

Interestingly, almost exactly the same processes occurred in the model (Fig. 7b,c and Fig. 9). The tight water vapor mixing ratio contours in the square of Fig. 7b indicated the outflow boundary to the north and the gust front to the south approaching to each other and they collided in Fig. 7c. The wind vectors in Fig. 7b and c showed this new cell initiation process as well. Fig. 9 shows this process in detail within the zoomed-in region shown by the black squared box in Fig. 7b. At 2300 (Fig. 9a), the two predicted outflow boundaries as indicated by bold dashed lines, are seen to almost match the observed ones (Fig. 8a). At 0000 (Fig. 9b), the cell (indicated by double arrows) triggered by the two bow-shaped outflow boundaries are almost exactly reproduced, so are the shape and location of the three outflow boundaries. The cell indicated by the large open arrow also matches observation at this time. By 0030, the western portion of the northward advancing boundary has collided with the northern one, and produced, as observed, a new cell, indicated by the large black arrow, and by 0100, this new cell as well as the eastern one intensified and the shape, intensity and location of these two cells match the observations almost exactly (Fig. 9d and Fig. 8d). These cells became the westward extension of cell group '4' (Fig. 7c), as observed (Fig. 3c).

In the next 2 hours from 0100, the model did not do a good job in organizing the cells into a squall line. The cells in group '4' that should have contributed to the western section of the squall line weakened subsequently and remained too far north, in northwest OK, while those that should make up the eastern section remained too far northeast, in the far southeast corner of KS (Fig. 7d). As will be shown in later sensitivity experiments, too strong southerly flow found in eastern OK

is at least partly responsible for the dislocation of the eastern part of the squall line.

In summary, experiment CNTL presented above which incorporated routine and special observations through hourly assimilation cycles successfully reproduced many of the observed characteristics of cell initiation in a complex mesoscale environment that involved an intensifying mesoscale low, a dryline, a cold front as well as an outflow boundary resulting from an earlier mesoscale convective system. The predicted location and timing of most of the cells agree rather well with observations, with CI timing errors being only about 10 minutes and location errors being less than 5 km for one cell group. The secondary cell initiation due to the collision between the pre-existing outflow boundary and the new gust front developing out of earlier dryline convection is also predicted very well by the model. The most significant problem is with the lack of organization of the cells into a solid squall line after 0010, or 7 hours into the prediction. The difficulty in maintaining the position of the initial outflow boundary to within northeastern Oklahoma in the model appears to have contributed to this problem, which appears to be related to the too strong southerly flow in that region. This issue will be explored through a sensitivity experiment that attempts to better analyze the initial cold pool behind the outflow boundary and one that uses a different eastern boundary location which results in a somewhat better flow prediction in eastern OK. Further, the 3-km model resolution may have been inadequate for the cell interaction and organization. The impact of higher resolution will be examined in Part II. The results of sensitivity experiments will be presented in the following sections.

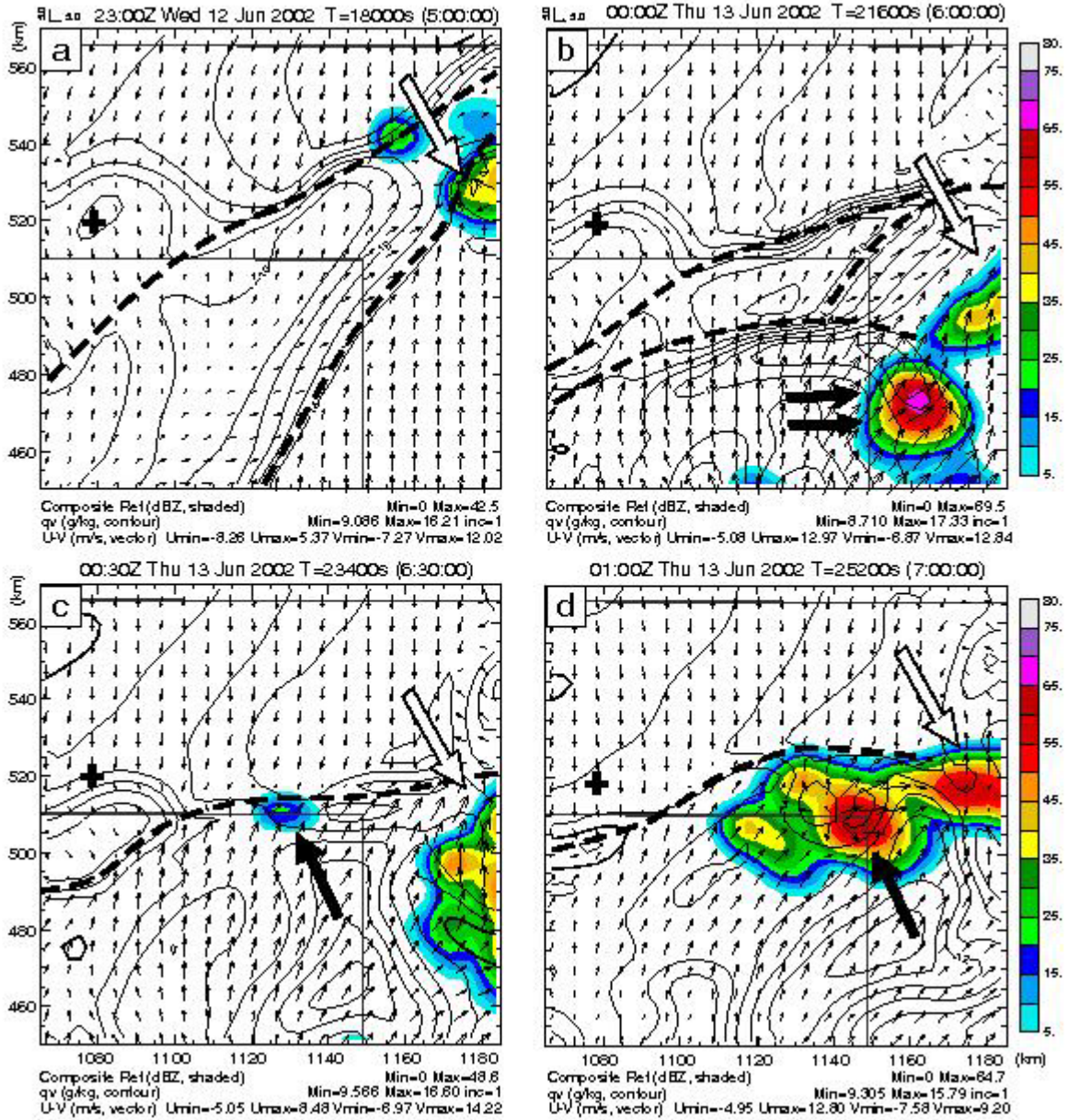


Fig. 9. As Fig. 7, but for a zoomed-in region shown by the black squared box in Fig. 7b and for times (a) 2300, 12 June 2002, (b) 0000, (c) 0030 and (d) 0100, 13 June 2002, that are close to the times of NCAR S-pol observations shown in Fig. 8. The '+' sign indicates the location of S-pol radar. The arrows point to convective cells to be discussed in the text and the bold dashed lines indicate the outflow convergence boundaries.

5. Results of sensitivity experiments

a. The impact of data assimilation length and frequency and the impact of special IHOP data

For high-resolution convective-scale prediction, special issues exist for arriving at the optimal initial condition. At such scales, conventional observational data, including those from mesoscale surface networks, usually do not have sufficient resolution to define

storm-scale features. Improper assimilation of such data sometimes can cause undesirable effects such as weakening existing convection in the background and introducing unbalanced noise. The simulation reported in XM06 used only a single 6-hourly assimilation cycle, and no impact of data assimilation was examined in that study. For the prediction of an isolated supercell storm event, Hu and Xue (2007) examined the impact of assimilation window length and assimilation intervals, for storm-scale radar data. The prediction results were found to be sensitive to the assimilation configurations.

Among all experiments presented in this paper, CNTL assimilates the most data (Table 2). Both standard and IHOP special observations (Table 1) are assimilated during a 6-hour time window at hourly intervals. To examine the impact of assimilation interval, we perform additional experiments 3HRLY and 6HRLY, in which both standard and special observations are assimilated, but at 3 hourly and 6 hourly intervals, respectively, over the same 6 hour period (between 1200 and 1800). In addition, in ‘cold-start’ experiment COLD, a single analysis without assimilation cycle is performed at 1800.

Another experiment, called STDOBS (Table 2), was also performed, which is the same as CNTL except for the exclusion of special data collected by IHOP. Here, the surface data routinely available from the Automated Surface Observing System (ASOS) and the Federal Aviation Administration’s (FAA) surface observing network (SAO data in Table 1), and the NWS radiosondes available twice daily and the hourly wind profiler network data are considered standard data. All other data listed in Table 1 are considered special data, including special soundings taken at 1500 and 1800. For all cases, 9-hour forecasts were performed, and the results are compared in terms of the prediction of CI and subsequent storm evolution.

Fig. 10 shows the model predicted fields of composite reflectivity, and surface water vapor mixing ratio and wind vectors from COLD, 3HRLY, 6HRLY and STDOBS, valid at 0100. It can be seen that the overall storm structure in COLD matches the observed reflectivity shown in Fig. 3c poorly (e.g., the convection in western TX is mostly missing) while those in the other three experiments match observations better, especially for the convection in northwest OK. However, unlike in CNTL, the initiation of new convection in eastern OK panhandle due to the collision of outflow boundaries (c.f., Fig. 7c) is missing in all of these experiments. In 6HRLY, the convection in western TX is over predicted (compare Fig. 10c and Fig. 3c) while in STDOBS, the convection is overall too strong. At the southwestern end of the overall system, the convection and the associated cold pool spread too far southeastward (Fig. 10d v.s. Fig. 3c), and the cold pool in northern OK and in KS appears to have also spread too far, creating two separate lines of cells along the gust fronts on its southeast and northwest sides. All other experiments predicted one dominant line of cells along the southern gust front as observed. Overall, the prediction of CNTL matches the observation best, at least at this time.

Table 2 lists the timing and location errors of the four primary cell initiations (‘CI1a’, ‘CI2’, ‘CI3’, ‘CI4’), as compared against radar observations. Here the timing of convective initiation is determined as the time of first significant radar echo or reflectivity exceeding 30 dBZ. It can be seen that in most cases, the model CI tends to be delayed compared to observations. In the case of COLD, CI1a, CI2 and CI4 are completely missing. In all other cases listed in the table, the model was able to predict all 4 CIs, although with different degrees of accuracy. Among the 5 experiments (CNTL, COLD, 3HRLY, 6HRLY and STDOBS), 3HRLY has the best timings for CI1a and CI4, STDOBS has the best timings with CI2 and CI3, while 6HRLY shares

the best timing for CI3 with STDOBS, and for CI4 with 3HRLY. CNTL has timing accuracies for CI1a and CI2 similar to the other experiments, but has delay in the initiation of CI3 and CI4 (2250 v.s. observed 2130 for CI3 and 2130 v.s. 2100 for CI4). The other three experiments predict the initiation of CI4 somewhat earlier instead. Overall, CI2 is best predicted; the presence of strong cold front-dryline forcing is probably the reason. The differences in the timing and location errors of CI1a among the successful experiments are also relatively small; again probably due to the strong dryline line forcing.

Intuitively, experiment CNTL assimilated the most data, so the final analysis at 1800 should be more accurate than those obtained using fewer data. We believe this is true for the analysis of mesoscale and synoptic scale features, including the dryline, outflow boundary, mesoscale low, and the broad flow pattern in general, as supported by the fact that the subsequent evolution of storms is predicted best in CNTL overall. Very frequent assimilation of mesoscale and synoptic scale observations do not, however, necessarily improve the analysis of *convective-scale* features or flow structures that are resolved by the high-resolution model grid in the background forecast because of the insufficient spatial resolutions of such data. In this case, the 3 km grid is able to resolve a significant portion of the *convective-scale* ascent forced by the horizontal convergence of the developing dryline and the outflow boundary, and by boundary layer convective eddies and rolls (c.f., XM06b). The analysis of mesoscale data, being of much coarser spatial resolutions (at $\sim 30 - 100$ km), tends to weaken low-level horizontal

convergence that develops in the model, hence weakening the forced ascent that is responsible for the triggering of convection.

A comparison between the forecast and an analyzed maximum vertical velocity time series from 1200 to 1800 in the regions where CI occurs later along the dryline, shows that the analyzed maximum vertical velocities are always less than those of the background forecast; i.e., the analysis reduces small-scale upward motion. We believe that the reduced ascent is partly responsible for the delay of CI4 and northward displacement of cells (because of the further northward retreat of the outflow boundary) in CNTL and in some of the other experiments, while the relatively coarse 3-km resolution is another major reason for the delay (Part II will show that the CI timing is much earlier when a 1 km grid is used). The dynamic consistency among the analyzed fields does not seem to be a major issue with the use of frequent hourly cycles.

The timing and location errors in STDOBS for CI1a and CI2 are similar to those of CNTL (Table 2). The predicted timing and location for CI3 and CI4 are better in STDOBS than in CNTL, however. For CI3, the timing error is only about 10 minutes (2140 v.s. 2130) and location error is less than 10 km, while for CI4, the timing error is 20 minutes (2040 v.s. 2100) and the location error is less than 5 km. The prediction of these two CIs is much better than that of CNTL, which has a significant delay in both CIs. The prediction of the convective storm evolution at later times in STDOBS is not better than in CNTL, however, as discussed earlier; there is a significant over-prediction of convection at, e.g., 0100 (Fig. 10).

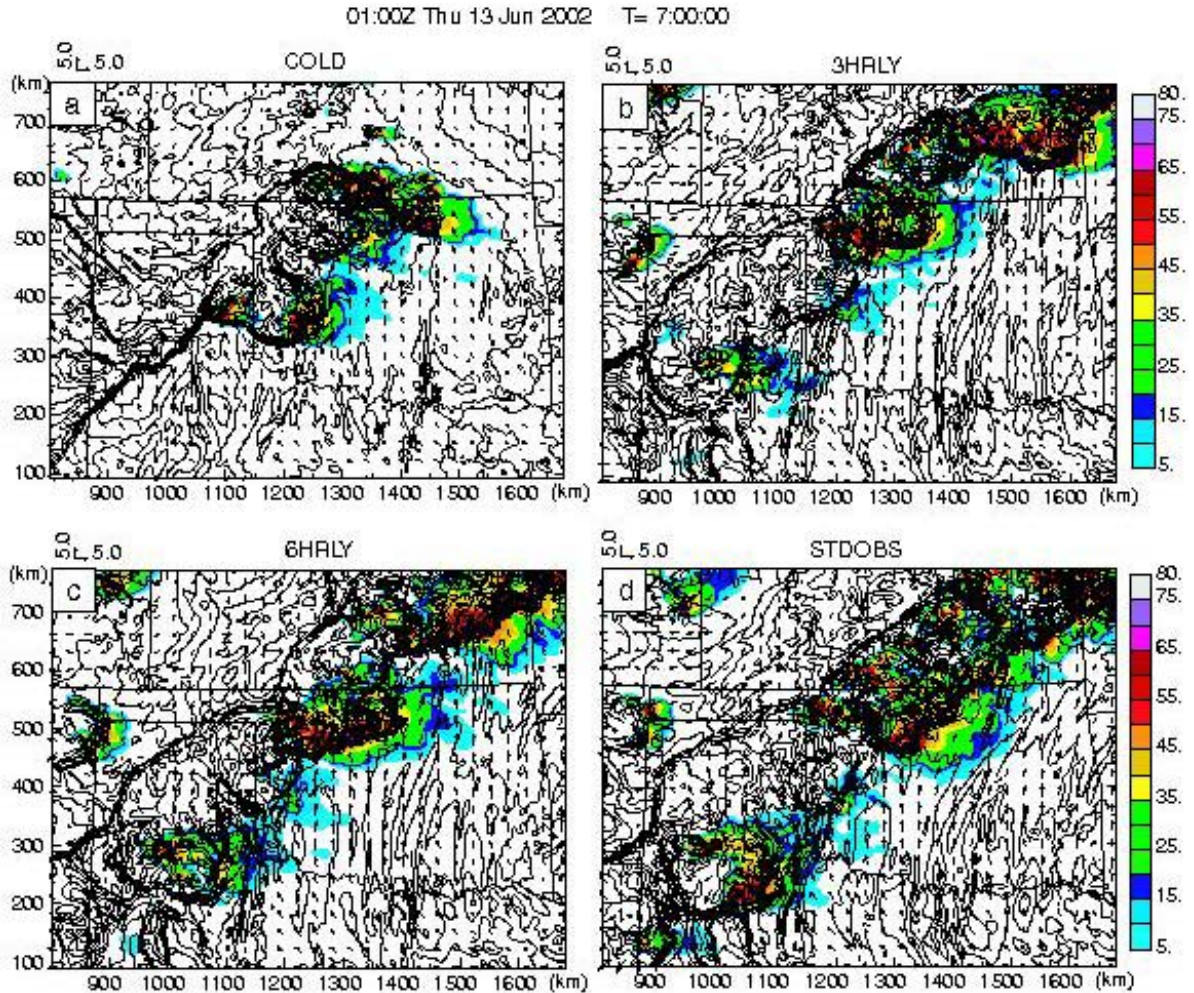


Fig. 10. As Fig. 7c but for experiments (a) COLD, (b) 3HRLY, (c) 6HRLY and (d) STDOBS, at 0100, 13 June, 2002.

Cell group ‘4’ was initiated near the dryline-outflow boundary ‘triple’ point, which was the focal point of intensive observation during IHOP_2002. The actual initiation was to the southeast of the triple point, however. Further, it is not obvious from the CAPE/CIN map (Fig. 2) that CI is preferred there. To better see how and why cell group ‘4’ is initiated in the model, we plot in Fig. 11 the horizontal convergence (gray shading), specific humidity, temperature and wind fields at the surface for CNTL, 3HRLY, 6HRLY and STDOBS at their times of first cloud formation, for a small domain around CI4. The first cloud formation is determined as the time when the 0.1 g kg^{-1}

contours of column maximum total condensate first appear within the plotting domain, which are shown as bold solid contours in the plots. Also overlaid in the plots are composite reflectivity contours for precipitation that first appear later on out of the initial clouds. We refer to such reflectivity as first echo. The times of first clouds are close to 2020, 2010, 2000 and 1950 for CNTL, 3HRLY, 6HRLY and STDOBS, respectively, while the corresponding times of first echo or CI are 2130, 2050, 2050 and 2040, as discussed earlier. The observed CI is at 2100. The maximum timing difference among the experiments is 30 minutes for the

first cloud and that for first echoes is 50 minutes.

The general surface flow patterns at the time of first cloud are similar between CNTL and STDOBS (Fig. 11a and Fig. 11d) while those of 3HRLY and 6HRLY are similar to each other (Fig. 11b and Fig. 11c). For CNTL and STDOBS, the line of strong wind shift between southerly flow ahead of and the easterly or northeasterly flow behind the outflow boundary is located near OK-KS border, in a east-west orientation, while those in 3HRLY and 6HRLY are in a more northeast-southwest orientation, located further north. It is believed that the hourly assimilation cycles helped improve the low-level flow analysis in CNTL and STDOBS.

The wind shift or shear line corresponds to a zone of enhanced convergence. South of this shear line in the generally southerly flow, fine-scale convergence bands are clearly evident in all 4 experiments, with the orientation more or less parallel to the low level winds. These bands are associated with boundary horizontal convective rolls and eddies; the interaction of these bands can create localized convergence maxima that form preferred locations of convective initiation (XM06b). Apparently, in all four cases, the first cloud (indicated by the bold solid contours in Fig. 11) is found directly over or very close to the localized convergence maximum (spots of enhanced gray) that is closest to the warm and moist air coming from the south or southeast. The convergence maxima located further west or north do not trigger convection as early or not at all because of lower values of low-level moisture and/or temperature there.

The location of first cloud in CNTL almost exactly coincides with the observed first echo (marked by 'x' in Fig. 11) while the first clouds in the other three experiments are located within 30 km of this location. The ensuing first echoes developed at different rates, with that in CNTL being the slowest (taking 70 minutes until 2130), and those in the

others taking 40 to 50 minutes. In CNTL, 3HRLY and 6HRLY, the first echoes are found to the northeast of the corresponding first clouds, while that in STDOBS is found to the north of the first cloud. These relative locations indicate the direction of cloud and cell propagation, which is to a large degree controlled by the horizontal winds that advect them. The complexity of the first cloud formation and the subsequent development of the first echo, in terms of the location relative to the primary outflow boundary convergence and maximum convergence centers due to boundary layer convective activities, suggest a degree of randomness. We leave the discussion on the exact processes of CI to Part II.

As discussed earlier, among experiments CNTL, 3HRLY, 6HRLY and STDOBS, the initiation of CI4 occurred the earliest in STDOBS, at 2040, 20 minutes earlier than observed while that in CNTL occurred 30 minutes later than observed at 2130. Such timing differences can be explained by the fact that the surface relative humidity at the time of first cloud is the highest in north-central OK in STDOBS (Fig. 11), which has values of around 15 g kg^{-1} in the region (Fig. 11d) while in other cases the values are between 13 and 14 g kg^{-1} (see the highlighted dark contours in the plots). The surface temperatures in the region are much closer, all around 36 C° . Because CNTL, 3HRLY, 6HRLY assimilated Oklahoma Mesonet data (Brock and Fredrickson 1993; Brock et al. 1995), which enjoy good data quality, surface analyses using them should be more reliable than those from STDOBS. Another reason that the low level air of STDOBS is believed to be too moist is that there was some spurious light precipitation around 1800 in STDOBS in southwestern OK (not shown); the advection of moistened air would result in higher low level moisture in north-central OK. Therefore, the apparent better timing of CI4 initiation is not necessarily for the right reason.

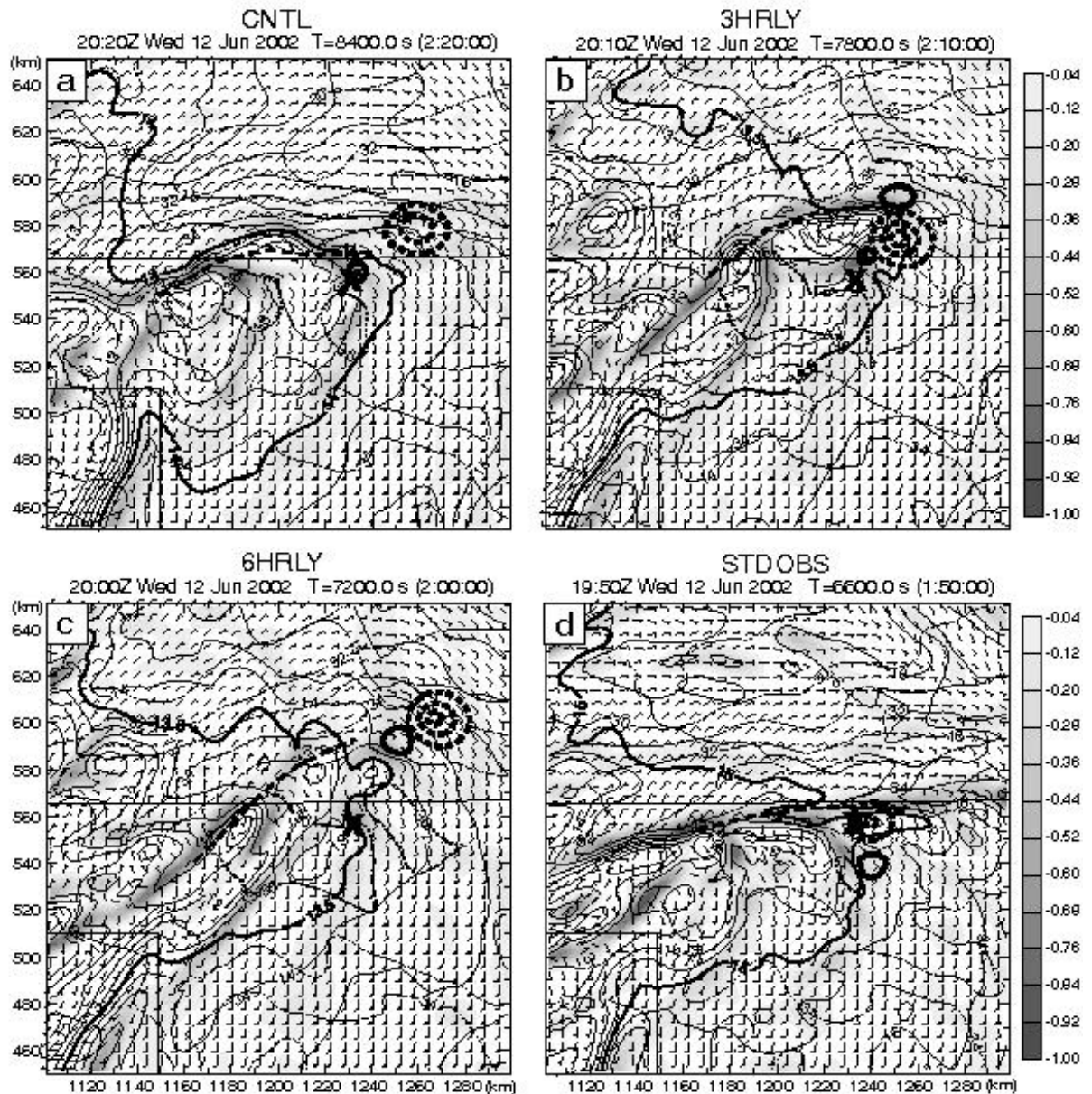


Fig. 11. Surface fields of horizontal divergence (only negative values shown in shaded gray), specific humidity (thin solid contours with 14, 13.5, 13.5 and 15 g kg⁻¹ contours highlighted by thicker lines in a, b, c and d, respectively), temperature (thin dashed contours with 36° C contours highlighted by thicker lines) and the 0.1 g kg⁻¹ contour of total condensed water/ice (bold solid contours) for experiments CNTL at 2020 (a), 3HRLY at 2010 (b), 6HRLY at 2000 (c) and STDOBS at 1950 (d), 12 June, 2002, which correspond to the times of first cloud formation in the experiments. The bold dashed contours are for composite reflectivity (10 dBZ intervals starting at 10 dBZ) when it first appears out of the initial clouds, at 2130, 2050, 2050, 2040 for the four experiments, respectively. The main wind shift or shear line associated with the outflow boundary is indicated by a thick dashed line in each plot. The location of observed CI4 is marked by an 'X' symbol.

b. Effect of vertical correlation scales in ADAS on the analysis and prediction of the cold pool

The outflow boundary created by the earlier MCS played an important role in this case, in helping initiate cell groups 4 and 5 and in the later organization of convection into a squall line. Earlier studies have shown the importance of properly initializing a cold pool for mesoscale prediction (Stensrud and Fritsch 1994; Stensrud et al. 1999). In our case, the ARPS Data Analysis System (ADAS) is used to analyze the surface and other observations. The ADAS is based on the Bratseth (1986) successive correction scheme and analyzes observations using multiple iteration passes. The spatial correlations scales of observations are empirically specified and usually change with data sources and iterations (Brewster 1996). Theoretically, spatial correlation scales should be based on flow-dependent background error covariance but such covariance is generally unavailable at the mesoscale. Because the choice of correlation scales is empirical, the impact of the choices should be investigated. For the analysis of cold pool, the vertical correlation scale is of particular interest.

The horizontal and vertical correlation scales used in CNTL and other experiments (except for ZRANGE) are listed in Table 3. The choice of these correlation scales is based on

additional experiments performed after the study of XM06, for the 24 May, 2002 case that focuses on convective initiation along a dryline; these values differ somewhat from those used in XM06. For the analysis of the cold pool behind the outflow boundary, the vertical scales ranging from 50 to 500 m used in CNTL appear too small for the surface data to properly reconstruct the cold pool, because too shallow a cold pool results. In experiment ZRANGE, larger vertical correlation scales of 800, 400, 300, 200 and 100 meters are used for the five successive passes. This results in a deeper vertical influence of surface observations and hence a deeper analyzed cold pool, as shown in Fig. 12 by the comparison of vertical cross-sections from CNTL and ZRANGE, in northeast OK along a line roughly normal to the outflow boundary (as indicated in Fig. 5d). It is clear from Fig. 12 that the analyzed cold pool is deeper in ZRANGE (Fig. 12b v.s. Fig. 12a), and is maintained longer in the forecast, as seen from both of its depth and horizontal extent (Fig. 12c through 10f). The deeper cold pool in this region helped create a strong convergence further west along the outflow boundary as the cold air is advected west-northwestwards (c.f., Fig. 5), resulting in a somewhat earlier and better timing of the initiation of cell group 4 (Table 2) than in CNTL.

Pass number	Analyzed observations	Horizontal filter length scale (km)	Vertical filter length scale (m)
1	raob, wpdn, comp,mdcrs	320	500
2	raob, wpdn, comp, mdcrs, sao	160	100
3	sao, coag, okmeso, swks, wtx, gwmd	80	100
4	sao, coag, okmeso, swks, wtx, gwmd	50	50
5	coag, okmeso, swks, wtx, gwmd	30	50

Table 3. List of analyzed observations and the horizontal and vertical correlation scales used by each pass of the ADAS analysis in all experiments except for ZRANGE.

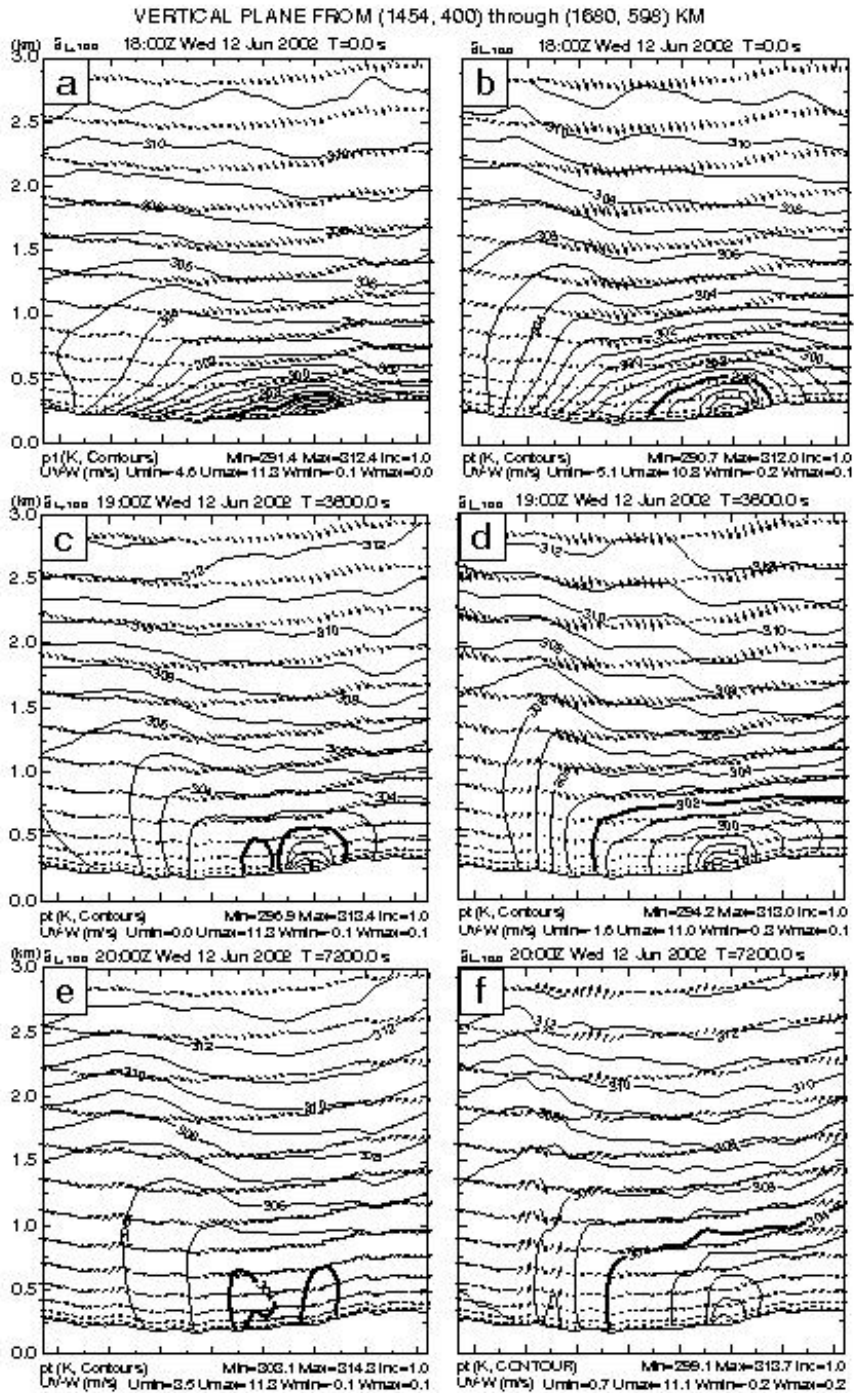


Fig. 12. Vertical cross-sections of potential temperature and wind vectors projected to the cross-section, through points (1454, 400) and (1680, 598) km, as indicated by the thick straight white line in Fig. 5d, at 1800 (upper panel), 1900 (middle panel) and 2000 (lower panels), for experiments CNTL (left panels) and ZRANGE (right panels). Certain characteristic contours are highlighted as bold to facilitate comparison.

However, this set of larger vertical correlation scales did not lead to a better prediction of the initiation of all of the other cell groups, nor of the general evolution of convection. This suggests that the increased vertical correlation scales do not necessarily improve the analysis in other regions outside the cold pool. For truly optimal analysis, flow-dependent background error correlation scales have to be estimated and used. Such flow-dependent statistics will require more sophisticated assimilation methods such as the ensemble Kalman filter (Evensen 1994).

c. Impact of lateral boundary locations

For limited area simulation and prediction, the location of the lateral boundaries and the specification of lateral boundary conditions have a significant impact (Warner et al. 1997). In this study, the lateral boundary conditions are obtained from the Eta realtime analyses at 6 hour intervals, and from interleaved 3-hour forecasts. They are linearly interpolated to the model time and spatially interpolated to the 3-km resolution grid. In 2002, the horizontal resolution of the operational Eta forecasts was 12 km and the data used in this study had been interpolated to a 40 km grid with 39 pressure levels before downloading from NCEP. For the experiments reported earlier, a rather large computational domain, as shown in Fig. 4, is used. This choice was based on some initial experiments where sensitivity to the lateral boundary location was found. In this subsection, some of the sensitivities of CI and later evolution of convection to the boundary location are documented.

In general, the upstream boundary conditions have the most significant impact on model simulation or prediction. In our case, there exists a significant flow response to the day time heating over the sloping terrain in the TX panhandle area. Between 1200 and 1800, the flow ahead (east) of the dryline turned from south-southwesterly into south-southeasterly, as

a response to the elevated heating and to the tightening mesoscale low circulation in the OK panhandle (c.f., Fig. 5). In our initial experiments, a smaller domain was used, as shown by the box in Fig. 4. With this smaller domain, the western boundary is located just west of the NM-TX border and the southern boundary is about 200 km north of the larger domain boundary. In experiment SML (Table 2), the same configurations, including the assimilation cycles, as CNTL are used, except for the use of this smaller domain. In this case, the westerly winds behind the dryline are found to be too strong (which mostly came from the lateral boundary condition), and the upslope acceleration east of the dryline is too weak, causing the dryline to propagate too far to the east. Consequently, the storms along the southern portion of the dryline also propagated too far to the east (Fig. 13). The too weak upslope flow was related to the fact that the southern boundary was located within the region of flow response. A separate experiment in which the southern boundary alone was placed further south, to a location similar to that of CNTL, a much stronger upslope response was obtained (not shown). The strong westerly winds behind the dryline in SML also enhanced the convergence along the dryline, resulting in earlier initiation of cell groups 1a and 2 (Table 2 and Fig. 13a) than in CNTL. The initiation of group 3 was affected by the too far eastward propagation of cell group 2 (Fig. 13b).

To see if the upslope flow was a response to the elevated heating or to the dryline convection, we performed an alternative experiment to CNTL, in which the moist processes were turned off. In that case, the upslope flow response was found to be as strong as in the moist case, suggesting that convective heating did not play a major role.

The location of the eastern boundary of the model also affects our simulations in a significant way, especially in terms of the winds in northeast OK, northwest AR and southeast KS that are associated with the cold outflow

from the MCS passing through that region earlier in that day (see Introduction). When the eastern boundary is located just east of the OK-AR border in SML, a strong southeasterly component of winds through the OK-AR border into the northeastern OK region is maintained into the later period of simulation (Fig. 13b,c,d), which actually verified well against OK Mesonet data (not shown). This southeasterly flow is maintained as a result of spreading cold outflow from the MCS in AR. This particular feature is not handled well in all experiments that use the larger domain; in fact, a slightly westerly wind component develops early in all the simulations (e.g., Fig. 7) and persists in northeast OK and southeast KS. This deficiency is at least partly responsible for the poor organization of convection at the later stage of forecast in CNTL (Fig. 7) and for the generally northeastward dislocation of convection (c.f. Fig. 7d and Fig. 3d). Actually, in SML, despite the much poorer evolution of

the earlier convection starting from the dryline (which should have mostly dissipated by 0100 anyway, c.f. Fig. 3d), the prediction of convective organization into a squall line is actually better reproduced (compare Fig. 13d with Fig. 7d and Fig. 3d). The southeasterly inflow forced in from the eastern boundary against the convective outflow associated with the squall line is believed to have played a role in this.

In most cases, a larger high-resolution domain is preferred. However, in this case, the MCS that passed through southern KS, northeastern OK into AR was not represented in the model; hence the model, despite its high resolution, was incapable of correctly reproducing the later southeasterly flow. In SML, the use of analysis boundary conditions from Eta helped capture this feature, resulting in a better prediction of convection in this region at the later time.

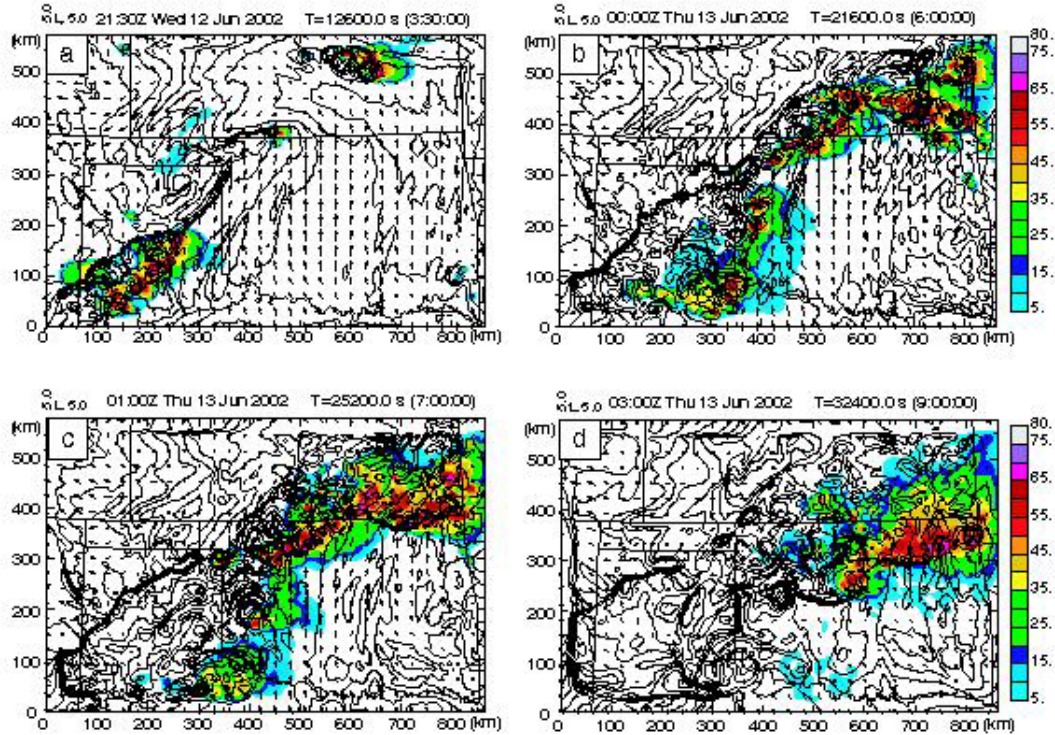


Fig. 13. As Fig. 7 but for small-domain experiment SML, at (a) 2130, (b) 0000, (c) 0100, and (d) 0300, 13 June, 2002.

6. Summary

The non-hydrostatic ARPS model with 3-km horizontal resolution is used to numerically simulate the 12-13 June 2002 case from the IHOP_2002 field experiment that involved initiation of many convective cells along and near a dryline and/or outflow boundary. The ARPS Data Analysis System (ADAS) is used for the data assimilation. The initial condition of the control experiment is generated through hourly intermittent assimilations of routine as well as non-standard surface and upper-air observations collected during IHOP_2002 from 1200 to 1800. The model is then integrated for 9 hours, spanning the hour before the first observed convective initiation along the dryline through the mature stage of a squall line organized from a number of initiated cells. The forecast domain is chosen large enough to minimize any negative effects from the lateral boundary.

As verified against multi-radar composite reflectivity fields, the model reproduced most of the observed convective cells with reasonably good accuracy in terms of the initiation timing and location, and predicted well the general evolution of convection within the first 7 hours of prediction. Detailed characteristics that were captured by the model include cell splitting, merger and regrouping, and the triggering of secondary convective cells by new outflow boundaries colliding with a pre-existing boundary. The main deficiencies of the prediction are with the organization of cells into a squall line and its propagation, during the last 2 hours of the 9-hour forecast, and the delay in timing of initiation in most cases.

Sensitivity experiments were performed to examine how the data assimilation intervals and non-standard observations influence the prediction of convective initiation and evolution. The results show that the experiment with 3-hourly assimilation cycles provides the best CI prediction overall while control

experiment with hourly assimilation intervals predicts the best convective evolution. The CI in the control experiment is delayed in general. Suggested causes are the insufficient spatial resolution and the typically damping effect on the forced ascent in the high-resolution forecast background when assimilating data that contain only mesoscale information. The apparent improvement to the timing of some of the CI in the experiment that did not include non-standard data is suggested to be due not necessarily to a better initial condition, but rather to the cancellation of resolution-related delay and the too moist initial condition at the low levels.

The vertical correlation scales used in ADAS which employs multi-pass successive corrections are shown to significantly impact the structure of the analyzed cold pool using surface observations. Larger vertical correlation scales resulted in a deeper cold pool that lasted longer, leading to stronger convergence and earlier initiation at the outflow boundary. Truly flow-dependent background error covariances will be needed to provide the best information on how the surface observation information should be spread in the vertical.

When the western boundary of the model grid was placed close to the southwest end of the dryline, apparently too strong westerly flow initiated convection at the dryline earlier, and helped push the convective cells too far to the east. When the southern boundary of the model grid is placed not far enough south, the upslope flow response east of the dryline is constrained significantly, reducing the easterly flow component needed to slow down the eastward propagation of the dryline and related convection. When the eastern boundary is placed near the Oklahoma-Arkansas border in order to bring in observed information of the spreading cold pool from the earlier mesoscale convection in Arkansas, the information helped improve the prediction of flow ahead of an

organizing squall line later into the prediction, hence leading to a better organized squall line.

Preliminary analyses of model results indicate that convection south of the outflow boundary is initiated where low-level localized convergence maxima are found. Boundary layer convective rolls and eddies clearly played important roles, as found in our earlier study (Xue and Martin 2006b). A more detailed analysis on the initiation mechanisms will be presented in Part II of this paper.

Acknowledgements

This work was mainly supported by NSF grants ATM-0129892 and ATM-0530814. M. Xue was also supported by NSF grants ATM-0331756, ATM-0331594, EEC-0313747, and by a grant from the Chinese Academy of Sciences (No. 2004-2-7). Dr William Martin is thanked for helping prepare the IHOP data and for proofreading the manuscript. Jian Zhang and Wenwu Xia of NSSL provided the mosaic reflectivity data and Dr. Ming Hu helped plot the mosaic data. Supercomputers at the Pittsburgh Supercomputing Center were used for most of the experiments.

References

- Benjamin, S. G., D. Devenyi, S. S. Weygandt, K. J. Brundage, J. M. Brown, G. A. Grell, D. Kim, B. E. Schwartz, T. G. Smirnova, T. L. Smith, and G. S. Manikin, 2004: An hourly assimilation-forecast cycle: The RUC. *Mon. Wea. Rev.*, **132**, 495-518.
- Bratseth, A. M., 1986: Statistical interpolation by means of successive corrections. *Tellus*, **38A**, 439-447.
- Brewster, K., 1996: Application of a Bratseth analysis scheme including Doppler radar data. Preprints, 15th Conf. Wea. Anal. Forecasting, Norfolk, VA, Amer. Meteor. Soc., 92-95.
- Brock, F. V. and S. Fredrickson, 1993: Oklahoma mesonet data quality assurance. Extended Abstracts, Eighth Symp. Meteorological Observations Instrumentation, Anaheim, CA, Amer. Meteor. Soc., 311-316.
- Brock, F. V., K. C. Crawford, R. L. Elliott, G. W. Cuperus, S. J. Stadler, H. L. Johnson, and M.D. Eilts, 1995: The Oklahoma Mesonet: A technical overview. *J. Atmos. Oceanic Tech.*, **12**, 5-19.
- Chou, M.-D., 1990: Parameterization for the absorption of solar radiation by O₂ and CO₂ with application to climate studies. *J. Climate*, **3**, 209-217.
- Chou, M.-D., 1992: A solar radiation model for use in climate studies. *J. Atmos. Sci.*, **49**, 762-772.
- Chou, M.-D. and M. J. Suarez, 1994: An efficient thermal infrared radiation parameterization for use in general circulation models. NASA Tech. Memo. 104606, 85 pp.
- Evensen, G., 1994: Sequential data assimilation with a nonlinear quasi-geostrophic model using Monte Carlo methods to forecast error statistics. *J. Geophys. Res.*, **99(C5)**, 10 143-10 162.
- Fritsch, J. M. and R. E. Carbone, 2004: Improving quantitative precipitation forecasts in the warm season: A USWRP research and development strategy. *Bull. Amer. Meteor. Soc.*, **85**, 955-965.
- Hu, M. and M. Xue, 2007: Impact of configurations of rapid intermittent assimilation of WSR-88D radar data for the 8 May 2003 Oklahoma City tornadic thunderstorm case. *Mon. Wea. Rev.*, **135**, 507-525.
- Lin, Y.-L., R. D. Farley, and H. D. Orville, 1983: Bulk parameterization of the snow field in a cloud model. *J. Climate Appl. Meteor.*, **22**, 1065-1092.

- Markowski, P., C. Hannon, and E. Rasmussen, 2006: Observations of convection initiation "failure" from the 12 June 2002 IHOP deployment. *Mon. Wea. Rev.*, **134**, 375-405.
- Stano, G., 2003: A case study of convective initiation on 24 May 2002 during the IHOP field experiment, M.S. Thesis, School of Meteorology, University of Oklahoma, 106 pp.
- Stensrud, D. J. and J. M. Fritsch, 1994: Mesoscale convective systems in weakly forced large-scale environment. Part II: Generation of a mesoscale initial condition. *Mon. Wea. Rev.*, **122**, 2084-2104.
- Stensrud, D. J., G. S. Manikin, E. Rogers, and K. E. Mitchell, 1999: Importance of cold pools to NCEP mesoscale Eta model forecasts. *Wea. Forecasting*, **14**, 650-670.
- Sun, W.-Y. and C.-Z. Chang, 1986: Diffusion model for a convective layer. Part I: Numerical simulation of convective boundary layer. *J. Climate Appl. Meteor.*, **25**, 1445-1453.
- Warner, T. T., R. A. Peterson, and R. E. Treadon, 1997: A tutorial on lateral boundary conditions as a basic and potentially serious limitation to regional numerical weather prediction. *Bull. Amer. Meteor. Soc.*, **78**, 2599-2617.
- Weckwerth, T. M. and D. B. Parsons, 2006: A review of convection initiation and motivation for IHOP_2002. *Mon. Wea. Rev.*, **134**, 5-22.
- Weckwerth, T. M., H. V. Murphey, C. Flamant, C. R. Pettet, S. Bastin, and R. Wakimoto, 2005: Convection initiation on 12 June 2002 during IHOP_2002. . 11th Conf. Mesoscale Processes, Albuquerque, NM, Ameri. Meteor. Soc.
- Weckwerth, T. M., D. B. Parsons, S. E. Koch, J. A. Moore, M. A. LeMone, B. B. Demoz, C. Flamant, B. Geerts, J. Wang, and W. F. Feltz, 2004: An overview of the International H2O Project (IHOP_2002) and some preliminary highlights. *Bull. Amer. Meteor. Soc.*, **85**, 253-277.
- Wilson, J. W. and R. D. Roberts, 2006: Summary of convective storm initiation and evolution during IHOP: Observational and modeling perspective. *Mon. Wea. Rev.*, **134**, 23-47.
- Xue, M. and W. J. Martin, 2006a: A high-resolution modeling study of the 24 May 2002 case during IHOP. Part I: Numerical simulation and general evolution of the dryline and convection. *Mon. Wea. Rev.*, **134**, 149-171.
- Xue, M. and W. J. Martin, 2006b: A high-resolution modeling study of the 24 May 2002 case during IHOP. Part II: Horizontal convective rolls and convective initiation. *Mon. Wea. Rev.*, **134**, 172-191.
- Xue, M. and H. Liu, 2007: Prediction of convective initiation and storm evolution on 12 June 2002 during IHOP_2002. Part II: High-resolution simulation and mechanisms of convective initiation. *Mon. Wea. Rev.*, To be submitted.
- Xue, M., J. Zong, and K. K. Droegemeier, 1996: Parameterization of PBL turbulence in a multi-scale non-hydrostatic model. Preprint, 11th AMS Conf. Num. Wea. Pred., Norfolk, VA, Amer. Meteor. Soc., 363-365.
- Xue, M., K. K. Droegemeier, and V. Wong, 2000: The Advanced Regional Prediction System (ARPS) - A multiscale nonhydrostatic atmospheric simulation and prediction tool. Part I: Model dynamics and verification. *Meteor. Atmos. Physics*, **75**, 161-193.
- Xue, M., D.-H. Wang, J.-D. Gao, K. Brewster, and K. K. Droegemeier, 2003: The Advanced Regional Prediction System

- (ARPS), storm-scale numerical weather prediction and data assimilation. *Meteor. Atmos. Physics*, **82**, 139-170.
- Xue, M., K. K. Droegemeier, V. Wong, A. Shapiro, K. Brewster, F. Carr, D. Weber, Y. Liu, and D.-H. Wang, 2001: The Advanced Regional Prediction System (ARPS) - A multiscale nonhydrostatic atmospheric simulation and prediction tool. Part II: Model physics and applications. *Meteor. Atmos. Phys.*, **76**, 143-165.
- Zhang, J., K. Howard, and J. J. Gourley, 2005: Constructing three-dimensional multiple-radar reflectivity mosaics: Examples of convective storms and stratiform rain echoes. *J. Atmos. Ocean. Tech.*, **22**, 30-42.